doi: 10.1093/pasj/xxx000

arXiv:1604.01884v1 [astro-ph.GA] 7 Apr 2016

Optical Variability Properties of Mini-BAL and NAL Quasars

Takashi HORIUCHI[1], Toru MISAWA[2], Tomoki MOROKUMA[3], Suzuka KOYAMADA[1], Kazuma TAKAHASHI[1] and Hisashi WADA[1]

[1]Department of Physics, Faculty of Science, Shinshu University, 3-1-1 Asahi, Matsumoto, Nagano 390-8621
[2]School of General Education, Shinshu University, 3-1-1 Asahi, Matsumoto, Nagano 390-8621
[3]Institute of Astronomy, Graduate School of Science, The University of Tokyo, 2-21-1 Osawa, Mitaka, Tokyo 181-0015

*E-mail: th.uchu.im@gmai.com

Received 2015 December 1; Accepted 2016 April 2

Abstract

While narrow absorption lines (NALs) are relatively stable, broad absorption lines (BALs) and mini-BAL systems usually show violent time variability within a few years via a mechanism that is not yet understood. In this study, we examine variable ionization state (VIS) scenario as a plausible mechanism, as previously suspected. Over three years, we performed photometric monitoring observations of four mini-BAL and five NAL quasars at $z_{\rm em} \sim$ 2.0 – 3.1 using the 105 cm Kiso Schmidt Telescope in u, g, and i-bands. We also performed spectroscopic monitoring observation of one of our mini-BAL quasar (HS1603+3820) using the 188-cm Okayama Telescope over the same period as the photometric observations. Our main results are as follows: (1) Structure function (SF) analysis revealed that the quasar UV flux variability over three years was not large enough to support the VIS scenario, unless the ionization condition of outflow gas is very low. (2) There was no crucial difference between the SFs of mini-BAL and NAL quasars. (3) The variability of the mini-BAL and quasar light curves was weakly synchronized with a small time delay for HS1603+3820. These results suggest that the VIS scenario may need additional mechanisms such as a variable shielding by X-ray warm absorbers.

Key words: galaxies: active — quasars: absorption lines — quasars: individual (HS1603+3820, Q1157+014, Q2343+125, UM675, Q0450-1310, Q0940-1050, Q1009+2956, Q1700+6416, and Q1946+7658)

1 Introduction

Quasars are useful background sources when investigating objects along our lines of sight. The absorption features in quasar spectra (i.e., quasar absorption lines; QALs) are usually classified into *intervening* QALs, which originate in intervening galaxies and the intergalactic medium, and *intrinsic* QALs, whose origin is physically associated to the background quasars. The latter comprise the accelerated gas outflow from the quasars themselves.

The gas outflow can be accelerated by several possible mechanisms: radiation pressure in the lines and continuum (Murray et al. 1995; Proga et al. 2000), magnetocentrifugal force (Everett 2005), and thermal pressure (Chelouche & Netzer 2005). However, the primary mechanism of the gas outflow is poorly understood. The outflow winds are important because (1) they eject angular momentum from the quasar accretion disk and promote accretion of new gas (Murray et al. 1995; Proga et al. 2000), (2) they expel large amounts of energy and metallicity, thus contributing to the chemical evolution of the local universe (Moll et al. 2007; Di Matteo et al. 2005), and (3) they

© 2014. Astronomical Society of Japan.

regulate star formation in nearby interstellar and intergalactic regions.

Broad absorption lines (BALs), defined as lines with a full width at half maximum (FWHM) exceeding 2,000 km s^{-1} (Weymann et al. 1991), have been routinely used in outflow wind studies. However, the line parameters (e.g., column density and line width) of BALs cannot be measured by model fitting because the line profiles are hopelessly blended and saturated. On the other hand, mini-BALs (with FWHMs of 500 — 2,000 km s^{-1}) and narrow absorption lines (NALs; with FWHMs $\leq$ 500 km s^{-1}) contain internal structures that can be model-fitted to probe their properties (e.g. Misawa et al. 2005, 2007b). The observed BALs, mini-BALs, or NALs depend on the viewing angle to the outflow stream (Murray et al. 1995; Ganguly et al. 2001). The detection rates of BALs, mini-BALs, and NALs are $\sim$10-15%, $\sim$5%, and $\sim$50%, respectively (Hamann et al. 2012), which probably indicate the global covering fraction of the absorbers around the continuum sources.

Around 70 – 90% of BALs are time-variable within 10 years (Gibson et al. 2008; Capellupo et al. 2011, 2012, 2013). As an extreme case, the measured C IV BAL variability of SDSSJ141007.74+541203.3 is only 1.20 days in the quasar rest-frame (Grier et al. 2015) representing the shortest timescale of absorption line variability ever reported. Recently, Misawa, Charlton and Eracleous (2014) monitored the spectra of mini-BAL and NAL quasars, and found that only the former shows significant time variability in its absorption lines.

However, the physical mechanisms of the absorption line variability remain unclear. To date, three scenarios have been proposed: (1) gas clouds crossing our line of sight (the gas motion scenario), (2) variable attenuation by flux that is redirected toward our line of sight by scattering material around the quasar (the reflection scenario), and (3) changing ionization levels in the outflow gas (the variable ionization state (VIS) scenario).

Misawa et al. (2005, 2007b) spectroscopically monitored the C IV mini-BAL in the quasar HS 1603+3820 for more than four years. They found multiple troughs in the mini-BAL that vary in concert. This finding eliminates the gas motion scenario (at least in 1603+3820) because it implies simultaneous crossing of gas clouds over our line of sight, which is unlikely. Misawa et al. (2010) also rejected the reflection scenario, because in spectropolarimetric observations of the same mini-BAL system, the fraction of polarized flux (i.e., the flux redirected by scattering material) is only $\sim$0.6 %, too small to support the reflection scenario. Gibson et al. (2008) found no correlations between quasars and absorption lines variability in 13 BAL quasars. On the other hand, Trévese et al. (2013) simultaneously monitored the equivalent widths (EWs) of BALs and the ultraviolet (UV) luminosities of their host quasars (i.e., ionizing photon density) and found clear correlations in a single quasar, supporting the VIS scenario. The VIS scenario has not been tested in mini-BAL / NAL quasars and is still being debated.

In this study, we verify the VIS scenario in the light curves of four mini-BAL quasars and five NAL quasars (hereafter, quasar variability[1]). We also search for possible correlations between the outflow and quasar parameters, as discussed in the literature (e.g. Giveon et al. 1999 (G99, hereafter); Vanden Berk et al. 2004 (VB04, hereafter); de Vries et al. 2005; Wold et al. 2007; Wilhite et al. 2008 (W08, hereafter); Meusinger & Weiss 2013). Section 2 of this paper describes the sample selection, observation, and data analysis. In Section 3, we present the photometric data of mini-BAL / NAL quasars. Section 4 discusses the viability of the VIS scenario in mini-BAL and NAL quasars and the possible correlations between parameters. Results are summarized in Section 5. Throughout, we adopt a cosmological model with H_0=70 km s^{-1} Mpc^{-1}, Ω_m=0.27 and Ω_Λ=0.73.

2 Observation and Data Analysis

2.1 Sample Selection

Our samples are selected based on availability of multi-epoch high dispersion spectroscopic studies in Misawa, Charlton and Eracleous (2014). We sampled four mini-BAL quasars (HS1603+3820, Q1157+014, Q2343+125, and UM675) and five NAL quasars (Q0450-1310[2] Q0940-1050, Q1009+2956, Q1700+6416, and Q1946+7658), whose absorption line variabilities (or non-variabilities) have been already studied by Misawa, Charlton and Eracleous (2014) using Subaru with the High Dispersion Spectrograph (HDS, $R \sim$ 45,000), Keck with the High Resolution Echelle Spectrometer (HIRES, $R \sim$ 36,000), and Very Large Telescope (VLT) with the Ultraviolet and Visual Echelle Spectrograph (UVES, $R \sim$ 40,000) in time intervals of $\sim 4 - 12$ years. Our sample quasars are summarized in Table 1.

2.2 Imaging Observations

Photometric observations were performed by the 105-cm Kiso Schmidt Telescope with a Kiso Wide Field Camera (KWFC, Sako et al. 2012). The eight 2K$\times$4K charge coupled devices (CCDs) in the KWFC provides a field-of-view (FoV) of 2.2° $\times$ 2.2°. Since five of our nine quasars are located in the Sloan digital sky survey (SDSS) field, our photometry used the SDSS (u, g, and i) filters instead of the Johnson filters. Moreover, as the u-band is less sensitive than the g- and i-bands, we adopted a 2 $\times$ 2 binning mode (1.89 arcsec/pixel) for the u-band observations.

The quasars were repeatedly observed from April 14, 2012

[1] On the other hand, changes in the absorption strength/feature are referred to as the "absorption line variability"

[2] Although this quasar was not studied in Misawa, Charlton and Eracleous (2014), we sampled it because it hosts a reliable *intrinsic* NAL confirmed by (Misawa et al. 2007a).

to October 16, 2014, with a typical monitoring interval of three months, representing the typical variability time scale of BALs (e.g., Capellupo et al. 2011, 2012, 2013). Observation logs of the individual quasars are summarized in Table 2. The log excludes Q0450-1310 and Q1946+7658 in the u-band because the continuum fluxes of these quasars are heavily absorbed by the foreground intergalactic medium (i.e., Lyα forest). Bias subtraction, flat-fielding, sky subtraction, and World coordinate system matching were performed by an automatic analysis pipeline. The same pipeline was used for supernova discoveries in the Kiso Supernova Survey (KISS) project (Morokuma et al. 2014).

2.3 Relative Photometry

The extraction and magnitude measurements of quasars and comparison stars were performed by SExtractor (Bertin & Arnouts 1996). Regions crowded with stars were selected by the flux estimation code `FLUX_BEST`.

Since we mainly investigate the light curves of quasars (i.e., the *relative* magnitudes between observing epochs), we do not need to measure their *true* magnitudes. Therefore, we performed relative photometry by simultaneously monitoring the quasars and *effective* photometric standard stars (hereafter called *comparison stars*) near the quasars. The comparison stars were selected as follows. We chose two (unsaturated) bright stars near the target quasars in the same CCDs and investigated their *relative* magnitudes Δm (= $|m_{s1} - m_{s2}|$), where m_{s1} and m_{s2} are the magnitudes of the bright stars. If their relative variability between the two stars $|\Delta m - \langle \Delta m \rangle|$, where $\langle \Delta m \rangle$ is the average value of all observations, was always below 0.05 mag and below the 3σ level of the photometric errors (i.e., Δm was very stable), one of the stars was designated a comparison star. Otherwise, we continued searching for stars that satisfied the above criteria. A single comparison star was used in all epochs, unless different stars in different filters were required.

The quasars were subjected to relative photometry against these comparison stars and were classified as variable stars if their magnitude changed by more than 3σ and 0.05 mag. The total photometric error $\sigma_{\rm qso}$ in the quasar photometry (in units of magnitude) is defined as

$$\sigma_{\rm qso}{}^2 = \sigma_{\rm ph}{}^2 + \sigma_{\rm star}{}^2, \tag{1}$$

where $\sigma_{\rm ph}$ is the photometric error in the epochs to be compared and $\sigma_{\rm star}$ is the weighted average of the variability of the comparison star, which is defined as

$$\sigma_{\rm star} = \frac{\sum_{i,i<j} |\Delta m_i - \Delta m_j| w_{ij}}{\sum_{i,i<j} w_{ij}},\ w_{ij} = 1/{\sigma_{ij}}^2. \tag{2}$$

In Eq. (2), ${\sigma_{ij}}^2$ is the sum of squares of the photometric error in the comparison star between epochs i and j.

2.4 Properties of Sample Quasars

Table 1 lists the properties of our targets, namely, the quasar parameters (coordinates, emission and absorption redshifts, optical magnitudes, radio-loudness, bolometric luminosities, black hole masses, and Eddington ratios) and the absorption parameters (ejection velocities, whether lines are variable or not, averaged EWs, and variability amplitude of EWs). The last two parameters are measured for C IV absorption lines. These data were collected from literature or calculated from the reported data. After calculating the monochromatic luminosity at λ = 1450Å from the V-band magnitude, we applied the bolometric correction $L_{bol} \sim 4.4 \lambda L_{\lambda}$, following Narayanan et al. (2004). For the black hole mass, we used the heuristic equation of Vestergaard and Peterson (2006),

$$\log\left(\frac{M_{\rm BH}}{M_\odot}\right) = 0.660 + 0.53 \log\left(\frac{\lambda L_\lambda}{10^{44}\ {\rm erg/s}}\right) + 2\log\left(\frac{\rm FWHM}{\rm km\ s^{-1}}\right), \tag{3}$$

where the FWHM of the C IV broad emission line is measured from VLT/UVES archive spectra.

The quasar parameters of our targets were compared with those of ∼17,000 quasars at $z_{\rm em} \sim 2.0$ – 3.1 from the SDSS Data Release 7 (SDSS DR7) (see Figure 1). Our quasars demonstrate extremely large luminosity with a mean $\langle L_{bol} \rangle = 2.29 \times 10^{48}$ ergs s^{-1}. Eight of our quasars qualify as super Eddington with a mean Eddington ratio of $\langle \varepsilon \rangle = 3.02$, although their black hole masses are comparable to those of the SDSS quasars in the same redshift range. The mean quasar luminosity and Eddington ratio of SDSS DR7 (cataloged by Shen et al. 2011) are 5.13×10^{46} erg s^{-1} and 0.41 respectively.

The radio-loudness $R = f_\nu(5{\rm GHz})/f_\nu(4400{\rm Å})$ was also collected from the literature or calculated from FIRST radio measurements. Two quasars (Q1157+014 and UM675) are classifiable as radio-loud ($R > 10$; Kellermann et al. 1989), while the other 7 quasars are radio-quiet.

2.5 Spectroscopic Observation for HS1603+3820

We also performed spectroscopic monitoring observations of a single mini-BAL quasar (HS1603+3820) using the 188-cm Okayama Telescope with a Kyoto Okayama Optical Low-dispersion Spectrograph (KOOLS; Yoshida 2005). For these observations, we selected a VPH495 prism, which is sensitive to 4,500-5,400Å and a $1\farcs8$ slit (yielding R ∼1,100). The CCD was binned every 2×2 pixels.

Observations were performed from September 19, 2012 to May 21, 2015 over typical monitoring intervals of three months. Useful data were acquired on September 19 of 2012, May 30 of 2015, February 23 of 2015, and May 21 of 2015 (hereafter, these four periods are referred to as epochs 1, 2, 3, and 4). The observing log is listed in Table 3.

3 Results

This section present the photometric variability results of each quasar determined from light curves. The quasar variability properties of the mini-BAL and NAL quasars are then compared by SFs and color variability analysis. The results are summarized in Figures 2 and 3 and in Table 4.

3.1 Quasar variability

To examine the quasar variability of the nine mini-BAL / NAL quasars, we measured the standard deviation in the magnitude σ_m, the mean quasar variability $\langle|\Delta m|\rangle$, the maximum magnitude variability $|\Delta m|_{\rm max}$, the mean quasar variability gradient $\langle|\Delta m/\Delta t_{\rm rest}|\rangle$, and the maximum quasar variability gradient $|\Delta m/\Delta t_{\rm rest}|_{\rm max}$, following Borgeest and Schramm (1994) and G99. The mean values were calculated from all combinations of the observing epochs (e.g., from ${}_NC_2$ combinations , where N is the number of observing epochs.). The quasar variability gradient was defined as the quasar variability per unit time (year). These parameters are summarized in Table 4. The maximum quasar variability and its gradient are listed even if their significance level is below 3σ.

The most remarkable trend is the larger quasar variabilities in bluer bands than those in redder bands. This well-known property of quasars is repeatedly discussed in literature (e.g.,Cristiani et al. 1997; VB04; Zuo et al. 2012; Guo & Gu 2014). The largest quasar variabilities were exhibited by HS1603+3820 among the mini-BAL quasars ($|\Delta u_{\rm max}|$ ∼0.23) and by Q1700+6416 among the NAL quasars ($|\Delta u_{\rm max}|$ ∼0.30), while the largest variability gradients were exhibited by Q1157+014 among the mini-BAL quasars ($|\Delta i/\Delta t_{\rm rest}|_{\rm max}$ ∼5.0) and by Q1946+7658 among the NAL quasars ($|\Delta g/\Delta t_{\rm rest}|_{\rm max}$ ∼16.9).

3.2 Notes on Individual Quasars

HS1603+3820 (mini-BAL, z_{em}=2.542, $m_{\rm V}$=15.9) — This quasar exhibited a violently variable mini-BAL profile with an ejection velocity $v \sim$ 9,500 km s^{-1} (Misawa et al. 2007b). Among the mini-BAL quasars in the present study, this quasar showed the largest variability in the u-band ($|\Delta u| \sim 0.23$ mag) and the second largest variability in the g-band ($|\Delta g| \sim$ 0.19 mag) among our mini-BAL quasars. On the other hand, the mean and maximum quasar variability of HS1603+3820 were surprisingly small in the i-band (only ∼0.01 and ∼0.05 mag, respectively). For this quasar alone, we supplemented the photometric observations with spectroscopic observations. Obtained C IV mini-BALs in this quasar in each epochs are summarized in Figure 4, and we measured the EW of the C IV mini-BAL and monitored its variability. The results are summarized in Figure 5 and Table 5. The EW marginally varied between epochs 1 and 3 with absorption variability amplitude ΔEW = 6.0 ±4.2Å (significance level ∼1.5σ).

Q1157+014 (mini-BAL, z_{em}=2.00, $m_{\rm V}$=17.6) — This radio-loud quasar ($R = 471$) was the faintest among our sample quasars. At the start of our monitoring campaign, Q1157+014 showed a rapid quasar variability in the i-band with an amplitude $|\Delta i| \sim 0.14$ mag, much larger than those of the u- and g-band, between the first (April 2012) and second (May 2012) epochs. Thereafter, the magnitude variability remained high in the u-band and reduced in the i-band.

Q2343+125 (mini-BAL, z_{em}=2.515, $m_{\rm V}$=17.0) — This quasar exhibited the largest Eddington ratio ε among our mini-BAL quasars (ε ∼4.90) and the smallest mean quasar variability in the g-band ($\langle|\Delta g|\rangle \sim 0.02$). The quasar variability was only slightly larger in the i-band than in the g-band. Although Q2343+125 was observed only twice in the u-band, precluding an evaluation of its variability trend in that band, it appears that the quasar variability trends were consistent in all three bands.

UM675 (mini-BAL, z_{em}=2.15, $m_{\rm V}$=17.1) — This radio-loud quasar ($R = 438$) has a sub-Eddington luminosity (ε =0.91) and exhibited the largest variability in the g- and i-band among the mini-BAL quasars ($|\Delta g|$ and $|\Delta i|$ are ∼0.22 and 0.16 mag, respectively). Similar to Q2343+125, detailed trends in the u-band were precluded by the limited number of monitoring epochs.

Q0450-1310 (NAL, z_{em}=2.30, $m_{\rm V}$=16.5) — The magnitude of this quasar suddenly changed ($|\Delta g|$ ∼0.16 mag) in the g-band during the last three months of observations (from September 2013 to December 2013). The Δm in the g- and i-band largely differed from the 3rd to the 5th observing epochs, possibly because there were few observing epochs in the i-band.

Q0940-1050 (NAL, z_{em}=3.080, $m_{\rm V}$=16.6) — The g- and i-band fluxes monotonically decreased during the monitoring campaign. The quasar variability amplitudes of the all bands were almost identical. In this case, the variable trend in the u-band was obscured by the large photometric error, especially in the 2nd epoch. These errors were introduced by bad weather.

Q1009+2956 (NAL, z_{em}=2.644, $m_{\rm V}$=16.0) — Among our samples, this NAL quasar has the largest Eddington ratio (ε =7.21) and the smallest variability level in all bands ($|\Delta m| \leq 0.06$ mag).

Q1700+6416 (NAL, z_{em}=2.722, $m_{\rm V}$=16.13) — The bolometric luminosity and black hole mass of this quasar were the largest among our samples. Q1700+6416 also exhibited the largest u-band variability ($|\Delta u|$ ∼0.3 mag) among our samples.

Q1946+7658 (NAL, z_{em}=3.051, $m_{\rm V}$=15.85) — This quasar exhibited a cyclic quasar variability pattern with the highest half-year variability of the g-band magnitude in the quasar rest-frame ($|\Delta g|$ ∼0.24 mag). Conversely, the i-band magnitude was very stable over the same observation term.

3.3 Structure Function Analysis

We now examine the effects of time-scale and wavelength on the quasar variability properties. These relationships are usually determined through SF analysis. For this purpose, we adopt the Structure Function (SF) proposed by di Clemente et al. (1996),

$$S = \sqrt{\frac{\pi}{2}\langle|\Delta m(\Delta\tau)|\rangle^2 - \langle\sigma_n^2\rangle}, \quad (4)$$

where $|\Delta m(\Delta\tau)|$ and $\sigma_n = \sqrt{\sigma_{m_i}^2 + \sigma_{m_j}^2}$ are the magnitude variability and its photometric error, respectively, between two observing epochs separated by $\Delta\tau = t_j - t_i$ in the quasar's rest-frame. The bracket denotes the averaged value in paired observing epochs with time-lags within a specific range (after separation into four bins). Note that the wavelength coverage of the u-, g-, and i-band in the rest frame depends on the quasar redshift (see Figure 6). However, because the distribution of the emission redshift was $\sim$2.5 in two-thirds of our samples (six out of nine quasars), we can investigate the wavelength dependence of the SF. Detailed trends are investigated later in this subsection.

Figure 7 plots the SF as a function of time lag in the rest-frame for the u-, g-, and i-band. In all bands, the quasar variability increases with the time lag $\Delta\tau$. Because the observing epochs were fewer in the u- and i-band than in the g-band, they introduce larger errors in the SF. The SF is often fitted to a power-law (Hook et al. 1994; Enya et al. 2002; VB04; W08):

$$S_p(\Delta\tau) = \left(\frac{\Delta\tau}{\Delta\tau_p}\right)^{\gamma}, \quad (5)$$

where γ is the power-law index and the time scale $\Delta\tau_p$ defined such that $S_p(\Delta\tau_p)$ equals 1 mag. The fitting parameters to this model are summarized in Table 6. Note that because $\Delta\tau_p$ has an extremely large uncertainty, especially for small samples such as ours (see W08), we replace it by $S_p(\Delta\tau = 100$ days). The SFs were also fitted to the following asymptotic function (e.g., Trévese et al. 1994; Hook et al. 1994; Enya et al. 2002):

$$S_a(\Delta\tau) = V_a(1 - e^{-\Delta\tau/\Delta\tau_a}), \quad (6)$$

where V_a is the asymptotic value at $\Delta\tau = \infty$. Table 6 lists the best-fit parameters to this function, along with those of W08 and VB04. [3] In all cases, the quasar variability is higher at bluer than at redder wavelengths.

Finally, to examine the wavelength dependence of SF, we fitted the SF to the following equation (VB04):

$$S(\lambda) = A\exp(-\lambda/\lambda_0) + B, \quad (7)$$

where A, B and λ_0 are fit parameters. First, we separated our mini-BAL and NAL samples using a boundary time-lag of $\Delta\tau$ = 90 days[4] in the rest-frame, then fitted the subsamples to the above model. The fitting curves of our data and VB04's data are plotted in Figure 8. The quasar variability clearly decreases with wavelength, as noted in literature (e.g., G99; VB04; de Vries et al. 2005; Zuo et al. 2012). Moreover, the magnitudes of our SF are much lower than those of VB04's data because our mini-BAL / NAL quasars were much brighter than normal SDSS quasars in the same redshift range (Figure 1). The trend of the fitting reflects the anti-correlation between quasar variability and luminosity. No clear differences are observed between mini-BAL and NAL quasars.

[3] We emphasize that the rest-frame wavelength regions studied in the current work may differ from those in the literature.

[4] The average time lag of all combinations of observing epochs in all bands (used as the criterion).

3.4 Color Variability

Color variability is among the most remarkable properties of quasars. Although our relative photometry cannot determine the *true* magnitudes of quasars (see section 2.3), the color variability can be evaluated through the cancellation of photometry shifts (δm). For example, we can write

$$\Delta(u-g) = (u_2 + \delta u) - (g_2 + \delta g) - (u_1 + \delta u) + (u_1 + \delta g) \quad (8)$$
$$= u_2 - u_1 - (g_2 - g_1) \quad (9)$$
$$= \Delta u - \Delta g, \quad (10)$$

where the subscripts on u_1 and u_2 denote the first and second observing epochs in the comparison.

Figure 9 plots the $\Delta(u-g)$, $\Delta(u-i)$, and $\Delta(g-i)$ color variabilities as functions of quasar variability. The correlation properties of the mini-BAL and NAL quasars are summarized in Table 7. The color and magnitude variabilities are positively correlated in both mini-BAL and NAL quasars (namely, brighter quasars tend to be bluer; hereafter called the BWB trend). The same phenomenon has been reported in normal quasars (e.g. G99; Webb & Malkan 2000; VB04; Sakata et al. 2010, 2011; Kokubo et al. 2014). The correlation trends are consistent in the mini-BAL and NAL quasars.

The standard deviations of the quasar colors, the mean and maximum color variabilities, and the mean and maximum color variability gradients of the mini-BAL and NAL quasars, are listed in Table 8. Again, no significant differences exist between the mini-BAL and NAL quasars, except for 5.4σ difference in the maximum color gradient of $\Delta(u-i)$.

4 Discussion

4.1 Quasar Variability Trends of Mini-BAL and NAL Quasars

4.1.1 Structure Function

Comparing the SF fitting parameters of the mini-BAL and NAL quasars to those of normal quasars reported in VB04 and W08 (Table 6), we observe the following trends:

(i) The power-law indices γ of the mini-BAL and NAL quasars

($\gamma \sim$ 0.410±0.115, 0.264±0.056, and 0.436±0.115) were consistent with those of normal quasars reported in W08 (γ ∼0.43, 0.48, and 0.44) except in the g-band, although the rest-frame wavelength coverage differed among the quasar samples (being dependent on the redshift distribution of the quasar). Similar indices were obtained in a disk instability model [5] ($\gamma = 0.41 \sim 0.49$; Kawaguchi et al. 1998). No significant differences were observed between the mini-BAL and NAL quasars.

(ii) In the asymptotic model V_a, the asymptotic value at $\Delta\tau = \infty$ of mini-BAL / NAL quasars was approximately half that of normal quasars in the g and i-band. The same phenomenon was observed for $S(\Delta\tau = 100$ days).

4.1.2 Color variability

The mini-BAL and NAL quasars exhibit similar color-magnitude variability (Table 7) and color variability (Table 8) with one exception: a 5.4σ difference in the maximum color gradients (MCGs; $(|\Delta C/\Delta t_{\rm rest}|)_{\rm max}$).

The 5.4σ difference in MCGs was observed between a mini-BAL quasar (HS1603+3820) and a NAL quasar (Q1700+6416) with BWB trends in $\Delta(u-i)$. In both quasars, the variability was maximum in the u-band and moderate in the i-band. However, the $u-i$ variability developed over a shorter time - frame in Q1700+6416 than in HS1603+3820, which might explain the larger color variability gradient in the former than in the latter.

4.1.3 Correlation between EW and quasar variability

As shown in Figure 5, the variability trends of the magnitude and EW of the C IV mini-BAL for HS1603+3820 were marginally synchronized with the quasar variability leading the EW variability. Specifically, the EW first increased from 2012 September (epoch 1) to 2015 February (epoch 3) with a marginal significance level of $\sim 1.5\sigma$ ($\Delta{\rm EW} = 6.0 \pm 4.2$) and then decreased from 2015 February to 2015 May (epoch 4), while the quasar brightness in the u-band first decreased from 2012 September to 2014 May and then increased from 2014 May to 2015 May. The time-lag of the marginal synchronizing trend in quasar and absorption line variabilities is about nine months (∼2.6 months in the quasar rest-frame). If we assume the time-delay corresponds to the recombination time from C V to C IV, we can place a lower limit on the absorber's gas density as $n_e \geq 2.8 \times 10^4$ cm^{-3} by the same prescription as used in Narayanan et al. (2004).

Trévese et al. (2013) reported a similar synchronizing trend in a BAL quasar APM 08279+5255, although one of two NALs that are detected aside the BAL did not show such a synchronization. They suggested this was due to a larger recombination time for the NAL absorber with smaller electron density compared to the other absorbers. Both of these results are not inconsistent to the VIS scenario.

[5] Transient flares or blob formations caused by any instability should alter the luminosity.

4.2 The VIS Scenario

Assuming the VIS scenario, we now estimate the quasar variability that reproduces the observed absorption line variabilities of BAL and mini-BAL quasars reported in literature. If the VIS scenario holds, the absorption strengths will depend on the ionization condition of the absorber, which is quantified by the ionization parameter U

$$U \equiv \frac{1}{4\pi r^2 c n_e} \int_\nu^\infty \frac{L_\nu}{h\nu} d\nu = \frac{Q}{4\pi r^2 c n_e} = \frac{n_\gamma}{n_e}, \quad (11)$$

where Q is the number density of hydrogen-ionizing photons emitted from the continuum source per second, r is the distance between the absorber and the continuum source, and n_γ and n_e are the volume densities of the ionizing photons and electrons, respectively.

Here, we assume the absorption line variability of (mini-)BALs is attributed to recombination to (or ionization from) C^{2+} (*case A*, hereafter) and adopt the optimal ionization parameters for C^{2+} and C^{3+} ($\log$U ~ -2.8 and -2.0, respectively) (Hamann 1997). Because at least one of our mini-BAL quasars (HS1603+3820) is unlikely to vary by the gas motion scenario (Misawa et al. 2005, 2007b), we assume constant gas density n_e. Therefore, the ionizing photon density n_γ should increase/decrease by a factor of ∼6.3 to change $\log U$ from/to -2.8 to/from -2.0, corresponding to $\Delta m \sim 2$. For reference, a typical quasar varies by only $\Delta m \sim 0.1$ over several months and maximally varies by $\Delta m \sim 0.5$ over several years (Webb & Malkan 2000). These variabilities are much smaller than the above-required value[6].

However, C IV absorbers do not necessarily have an optimal ionization parameter for C^{3+} (i.e., $\log$U ~ -2.0). As the other extreme case, if mini-BAL absorbers have $\log$U ~ -3.0, their ionization fraction f (i.e., a fraction of Carbon in ion state C^{3+}) is very sensitive to the ionization parameter ($\Delta\log$f/$\Delta\log$U $\sim$ 1.8; *case B*, hereafter), although it weakly depends on the shape of incident ionizing flux. Indeed, the value of $\Delta\log$f/$\Delta\log$U for HS1603+3820, which is the only quasar among our sample for which the magnitude and EW of the C IV mini-BAL were simultaneously monitored over three years, is ∼1.1 between epochs 1 and 2 ($\Delta\log$EW $\sim \Delta\log$f ~ 0.1)[7] and ∼2.0 between the epochs 1 and 3 ($\Delta\log$EW ~ 0.18), assuming Δm ∼0.23 (the maximum quasar variability during our monitoring observations). These

[6] Even if we attribute the absorption line variability to recombination to (or ionization from) C V (whose optimal ionization parameter is $\log$U ~ -1.2), the required magnitude variability would be almost same.

[7] If absorbing clouds are optically thin (i.e., absorption lines are at a linear part of the curve-of-growth), $\Delta\log$EW is close to $\Delta\log$f, which is applicable for all mini-BALs in our sample except for one in Q1157+014.

values are expected for absorbers with ionization parameters of $\log U \sim -3 - -2$ (see Figure 2 of Hamann 1997). If this is the case, an averaged amplitude of absorption variability in four C IV mini-BALs in our sample ($\langle \Delta \log EW \rangle \sim \langle \Delta \log f \rangle \sim 0.1$) can be caused by only a small change of the ionizing flux, $\log U \sim 0.06$. This value corresponds to $\Delta m \sim 0.14$, comparable to a typical variability of our sample quasars as well as quasars in the literature (Webb & Malkan 2000). The variability amplitude of C IV ionizing photons in shorter wavelength ($\lambda_{\rm rest} \sim 200$ Å) may be even larger because of the anti-correlation between quasar variability and wavelength (see Section 3.3).

Thus, the case B is favorable for explaining the variability trend in HS1603+3820 with the VIS scenario. However, it has one shortcoming; four mini-BAL systems in our sample have either strong N V absorption lines or no remarkable Si IV absorption lines, which suggests their ionization condition is not as low as $\log U \sim -3$ (see Figure 2 of Hamann 1997). Therefore, it is less likely that the case B alone causes the absorption variability of mini-BALs in our sample quasars.

4.3 Additional mechanism to support the VIS Scenario

The outflow wind variability may be caused by more than one mechanism. We speculate that the VIS scenario is accompanied by an additional mechanism, such as variable optical depth between the flux source and the absorber. One promising candidates is a $warm\ absorber$ which has been frequently detected in X-ray spectroscopy (e.g.,Gallagher et al. 2002, 2006; Krongold et al. 2007; Mehdipour et al. 2012). Warm absorbers were originally proposed to avoid over-ionization of the outflow winds (Murray et al. 1995). Because warm absorbers are significantly variable in X-ray monitoring observations (e.g., Chartas et al. 2007; Giustini et al. 2010a, b), the ionization condition of the UV absorber in the downstream might also vary. Indeed, in a photoionization model, Różańska et al. (2014) estimated that the C IV mini-BAL absorber lies within r = 0.1 pc of the quasar center. Similarly, the X-ray warm absorber is estimated to be within 0.1 pc of HS1603+3820. Ganguly et al. (2001) argued that NAL and BAL absorbers locate at high and low latitudes above the accretion disk equator, respectively. A radiation-MHD simulation by Takeuchi, Ohsuga and Mineshige (2013) also predicts no warm absorbers at very high latitudes. If this picture is correct, X-ray shielding is ineffective in the NAL outflow directions. Supporting this idea, X-rays are not strongly absorbed in NAL quasars (Misawa et al. 2008). The model of Kurosawa and Proga (2009) supports that NAL absorbers are the interstellar media of host galaxies, which are swept up by the outflow wind. In this case, the absorbers should exhibit little variability because their volume density is very small (corresponding to a very long recombination time). Moreover, they are very distant (of the order of kpcs) from the continuum source, therefore they should be weakly influenced by the variable flux source. However, Hamann et al. (2013) find no evidence of strong X-ray absorption toward the outflows of either NAL or mini-BAL quasars. Instead of an X-ray warm absorber, they argue that small dense clumpy absorbers avoid over-ionization by self-shielding. In this case, we should expect no correlations between the absorption strengths of the UV and X-ray fluxes.

5 Summary

We performed i) photometric monitoring observations of four mini-BAL and five NAL quasars over more than three years and ii) spectroscopic observation for a single mini-BAL quasar (HS1603+3820) to investigate whether the VIS scenario can explain the absorption line variability in BALs and mini-BALs. Our main results are summarized below:

(1) Quasar variability increases with monitoring time-lag but decreases with observed wavelength, as previously reported in normal quasars.
(2) Mini-BAL and NAL quasars become bluer as they brightened (the BWB trend), as often observed in normal quasars.
(3) The quasar variability properties did not significantly differ between mini-BAL and NAL quasars, indicating that flux and color variabilities alone cannot account for the absorption line variabilities.
(4) Quasar magnitude was marginally synchronized with absorption strengths in one mini-BAL quasar HS1603+3820, with the former temporally leading the latter.
(5) The VIS scenario cannot causes the absorption variability of mini-BALs in our sample quasars unless the ionization condition of outflow gas is as low as $\log U \sim -3$.
(6) The VIS scenario may require an additional mechanism that regulates incident flux to the outflow gas. The most promising candidate is X-ray warm absorbers with variable optical depth.

Before conclusively validating the VIS scenario, we need to simultaneously monitor the outflow and shielding material by UV and X-ray spectroscopies. The presented monitoring observations should also be performed on quasars with a wide range of luminosities and Eddington ratios to mask the anti-correlation effect between the luminosity/Eddington ratio and quasar variability.

Acknowledgments

We thank Ken'ichi Tarusawa, Takao Soyano and Tsutomu Aoki for supporting our observations at Kiso Observatory for over three years. Ikuru Iwata and Hironori Tsutsui support our observations with the 188-cm Okayama Telescope with KOOLS. We also thank Noboru Ebizuka, Masami Kawabata and Takashi Teranishi for producing VPH grisms used

in KOOLS and kindly providing us, and Rina Okamoto for supporting our observations at Kiso Observatory and Okayama Astrophysical Observatory. The research was supported by JGC-S Scholarship Foundation and the Japan Society for the Promotion of Science through Grant-in-Aid for Scientific Research 15K05020.

References

Bertin, E., & Arnouts, S. 1996, A&AS, 117, 393
Borgeest, U., & Schramm, K.-J. 1994, A&A, 284, 764
Capellupo, D. M., Hamann, F., Shields, J. C., Halpern, J. P., & Barlow, T. A. 2013, MNRAS, 429, 1872
Capellupo, D. M., Hamann, F., Shields, J. C., Rodríguez Hidalgo, P., & Barlow, T. A. 2011, MNRAS, 413, 908
Capellupo, D. M., Hamann, F., Shields, J. C., Rodríguez Hidalgo, P., & Barlow, T. A. 2012, MNRAS, 422, 3249
Chartas, G., Brandt, W. N., Gallagher, S. C., & Proga, D. 2007, AJ, 133, 1849
Chelouche, D., & Netzer, H. 2005, ApJ, 625, 95
Cristiani, S., Trentini, S., La Franca, F., & Andreani, P. 1997, A&A, 321, 123
de Vries, W. H., Becker, R. H., White, R. L., & Loomis, C. 2005, AJ, 129, 615
di Clemente, A., Giallongo, E., Natali, G., Trevese, D., & Vagnetti, F. 1996, ApJ, 463, 466
Dietrich, M., Mathur, S., Grupe, D., & Komossa, S. 2009, ApJ, 696, 1998
Di Matteo, T., Springel, V., & Hernquist, L. 2005, Nature, 433, 604
Enya, K., Yoshii, Y., Kobayashi, Y., Minezaki, T., Suganuma, M., Tomita, H., & Peterson, B. A. 2002, ApJS, 141, 45
Everett, J. E. 2005, ApJ, 631, 689
Gallagher, S. C., Brandt, W. N., Chartas, G., & Garmire, G. P. 2002, ApJ, 567, 37
Gallagher, S. C., Brandt, W. N., Chartas, G., Priddey, R., Garmire, G. P., & Sambruna, R. M. 2006, ApJ, 644, 709
Ganguly, R., Bond, N. A., Charlton, J. C., Eracleous, M., Brandt, W. N., Churchill, & C. W. 2001, ApJ, 549, 133
Gibson, R. R., Brandt, W. N., Schneider, D. P., & Gallagher, S. C. 2008, ApJ, 675, 985
Giustini, M., Cappi, M., Chartas, G., Eracleous, M., Palumbo, G. G. C., & Vignali, C. 2010, Accretion and Ejection in AGN: a Global View, 427, 108
Giustini, M., Cappi, M., Chartas, G., Eracleous, M., Palumbo, G. G. C., & Vignali, C. 2010, IAU Symposium, 267, 397
Giveon, U., Maoz, D., Kaspi, S., Netzer, H., & Smith, P. S. 1999 (G99), MNRAS, 306, 637
Grier, C., et al. 2015, ApJ, 806, 111
Griffith, M. R., Wright, A. E., Burke, B. F., & Ekers, R. D. 1994, ApJS, 90, 179
Guo, H., & Gu, M. 2014, ApJ, 792, 33
Hamann, F. 1997, ApJS, 109, 279
Hamann, F., et al. 2013, MNRAS, 435, 133
Hamann, F., Simon, L., Rodríguez Hidalgo, P., & Capellupo, D. 2012, AGN Winds in Charleston, 460, 47
Hook, I. M., McMahon, R. G., Boyle, B. J., & Irwin, M. J. 1994, MNRAS, 268, 305
Just, D. W., Brandt, W. N., Shemmer, O., Steffen, A. T., Schneider, D. P., Chartas, G., & Garmire, G. P. 2007, ApJ, 665, 1004
Kawaguchi, T., Mineshige, S., Umemura, M., & Turner, E. L. 1998, ApJ, 504, 671
Kellermann, K. I., Sramek, R., Schmidt, M., Shaffer, D. B., & Green, R. 1989, AJ, 98, 1195
Kokubo, M., Morokuma, T., Minezaki, T., Doi, M., Kawaguchi, T., Sameshima, H., & Koshida, S. 2014, ApJ, 783, 46
Krongold, Y., Nicastro, F., Elvis, M., Brickhouse, N., Binette, L. Mathur, S., & Jiménez-Bailón, E. 2007, ApJ, 659, 1022
Kuhn, O., Bechtold, J., Cutri, R., Elvis, M., & Rieke, M. 1995, ApJ, 438, 643
Kurosawa, R., & Proga, D. 2009, ApJ, 693, 1929
Mehdipour, M., Branduardi-Raymont, G., & Page, M. J. 2012, A&A, 542, A30
Meusinger, H., & Weiss, V. 2013, A&A, 560, A104
Misawa, T., Charlton, J. C., & Eracleous, M. 2014, ApJ, 792, 77
Misawa, T., et al. 2007, ApJS, 171, 1
Misawa, T., Eracleous, M., Chartas, G., & Charlton, J. C. 2008, ApJ, 677, 863
Misawa, T., Eracleous, M., Charlton, J. C., & Kashikawa, N. 2007, ApJ, 660, 152
Misawa, T., Eracleous, M., Charlton, J. C., & Tajitsu, A. 2005, ApJ, 629, 115
Misawa, T., Kawabata, K. S., Eracleous, M., Charlton, J. C., & Kashikawa, N. 2010, ApJ, 719, 1890
Moll, R., et al. 2007, A&A, 463, 513
Morokuma, T., et al. 2014, PASJ, 66, 114
Murray, N., Chiang, J., Grossman, S. A., & Voit, G. M. 1995, ApJ, 451, 498
Narayanan, D., Hamann, F., Barlow, T., Burbidge, E. M., Cohen, R. D., Junkkarinen, V., & Lyons, R. 2004, ApJ, 601, 715
Proga, D., Stone, J. M., & Kallman, T. R. 2000, ApJ, 543, 686
Różańska, A., Nikołajuk, M., Czerny, B., Dobrzycki, A., Hryniewicz, K., Bechtold, J., & Ebeling, H. 2014, New, 28, 70
Sakata, Y., et al. 2010, ApJ, 711, 461
Sakata, Y., Morokuma, T., Minezaki, T., Yoshii, Y., Kobayashi, Y., Koshida, S., & Sameshima, H. 2011, ApJ, 731, 50
Sako, S., et al. 2012, SPIE, 8446, 6
Shen, Y., et al. 2011, ApJS, 194, 45
Takeuchi, S., Ohsuga, K., & Mineshige, S. 2013, PASJ, 65, 88
Trainor, R. F., & Steidel, C. C. 2012, ApJ, 752, 39
Trévese, D., Kron, R. G., Majewski, S. R., Bershady, M. A., & Koo, D. C. 1994, ApJ, 433, 494
Trévese, D., Saturni, F. G., Vagnetti, F., Perna, M., Paris, D., & Turriziani, S. 2013, A&A, 557, A91
Vanden Berk, D. E., et al. 2004 (VB04), ApJ, 601, 692
Véron-Cetty, M.-P., & Véron, P. 2010, A&A, 518, A10
Vestergaard, M., & Peterson, B. M. 2006, ApJ, 641, 689
Webb, W., & Malkan, M. 2000, ApJ, 540, 652
Weymann, R. J., Morris, S. L., Foltz, C. B., & Hewett, P. C. 1991, ApJ, 373, 23
Wilhite, B. C., Brunner, R. J., Grier, C. J., Schneider, D. P., & Vanden Berk, D. E. 2008 (W08) , MNRAS, 383, 1232
Wold, M., Brotherton, M. S., & Shang, Z. 2007, MNRAS, 375, 989
Wu, J., Charlton, J. C., Misawa, T., Eracleous, M., & Ganguly, R. 2010, ApJ, 722, 997
Yoshida, M. 2005, Journal of Korean Astronomical Society, 38, 117
Zuo, W., Wu, X.-B., Liu, Y.-Q., & Jiao, C.-L. 2012, ApJ, 758, 104

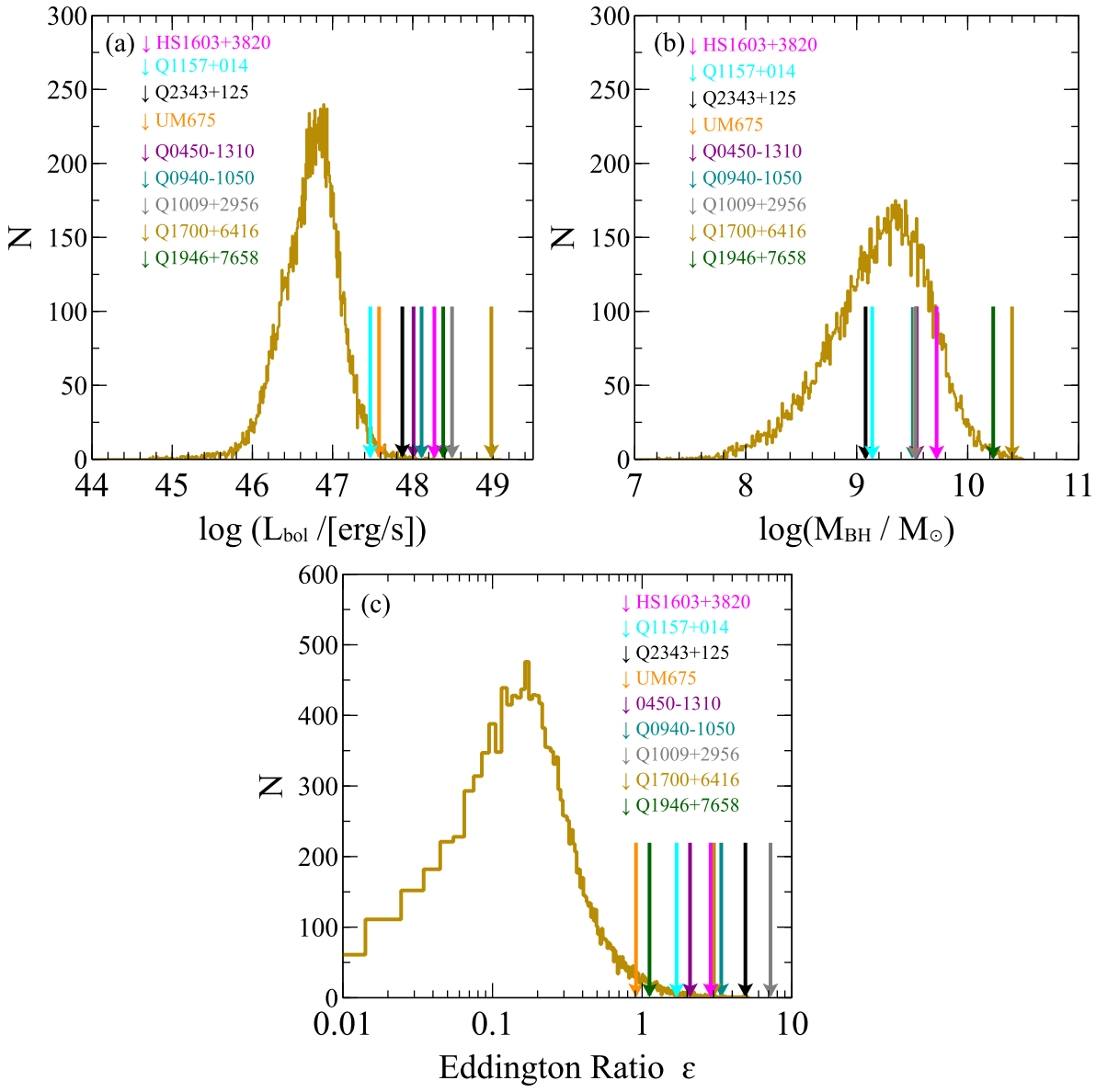

Fig. 1. (a) Distributions of bolometric luminosity, (b) virial black hole mass, and (c) Eddington ratio of our quasars (indicated by downward arrows) and ∼17,000 SDSS quasars at $2.0 \leq z < 3.1$ (Shen et al. 2011) (histograms). Exact values of these parameters for our nine quasars are presented in Table 1.

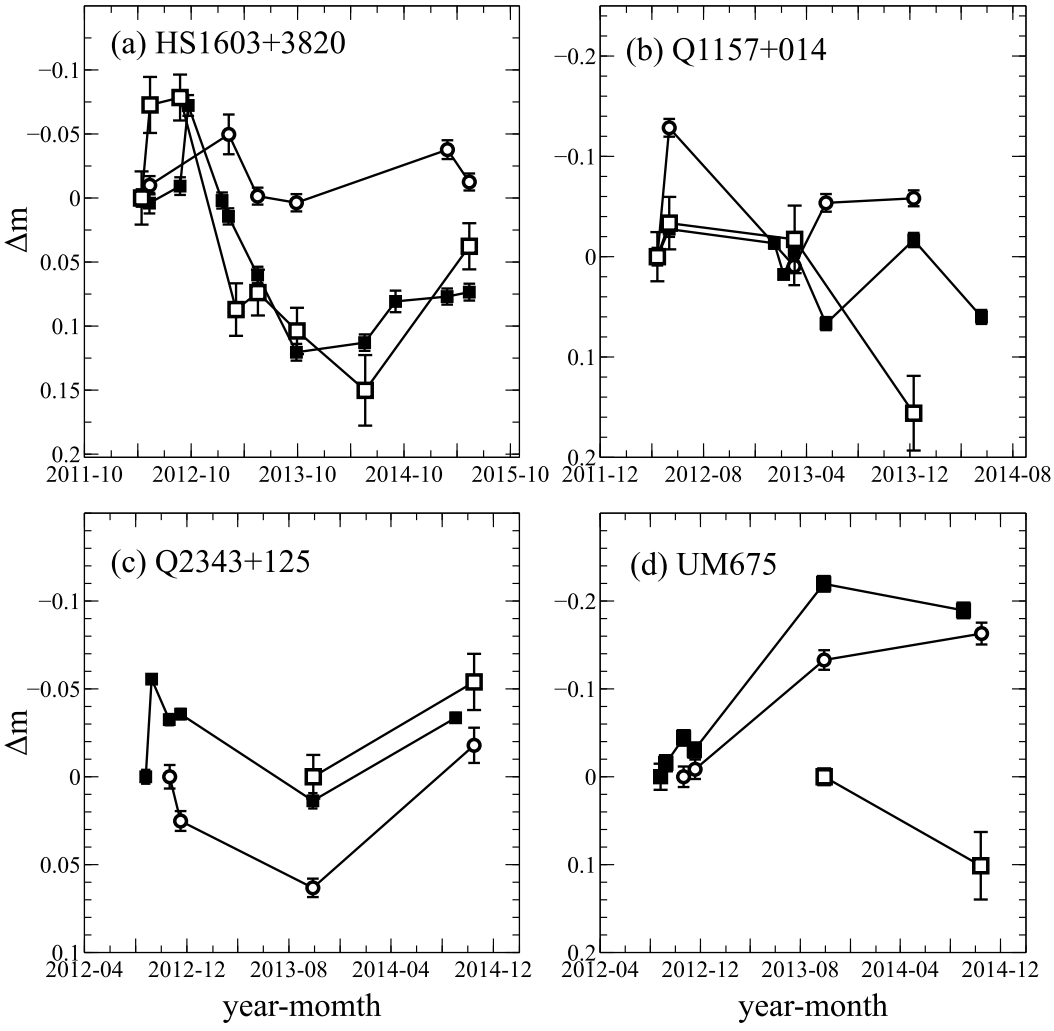

Fig. 2. Light curves of four mini-BAL quasars ((a) HS1603+3820, (b) Q1157+014, (c) Q2343+125, and (d) UM675), monitored in the u-band (*open squares*), g (*filled squares*), and i-band (*open circles*). The horizontal axis denotes the observing date (year-month) and the vertical axis Δm is the magnitude difference from the first observation. The Δm first observing epoch is zero by definition.

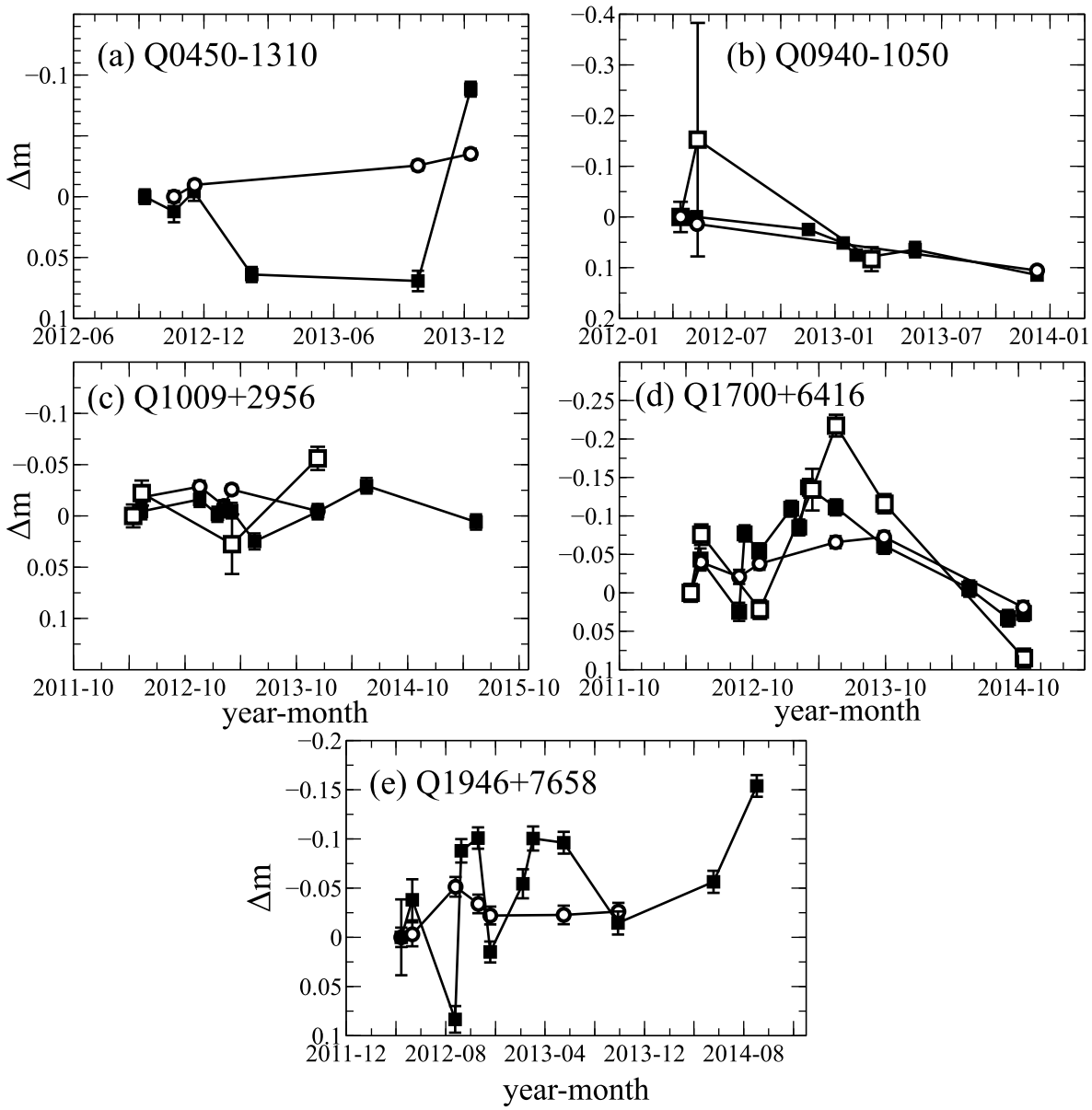

Fig. 3. Identical to Figure 2, but plotted for the five NAL quasars, (a) Q0450-1310, (b) Q0940-1050, (c) Q1009+2956, (d) Q1700+6416, and (e) Q1956+7658.

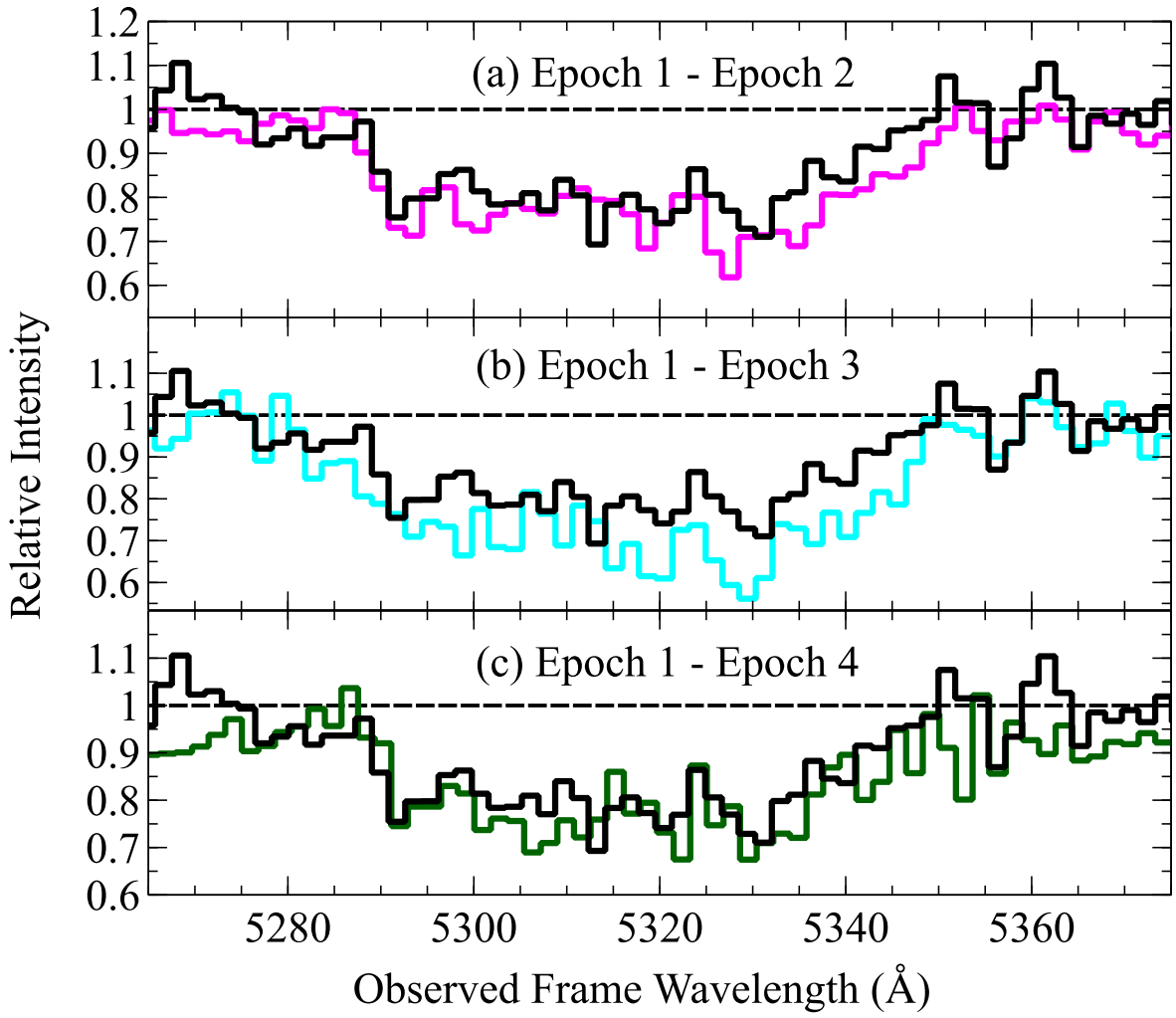

Fig. 4. Normalized spectra of HS1603+3820 around the C IV mini-BAL in observed frame taken with the 188-cm Okayama Telescope. $Black$, $magenta$, $cyan$ and $green$ histograms denote spectra taken on Sep 19, 2012 (epoch 1), May 30, 2014 (epoch 2), Feb 23, 2015 (epoch 3), and May 21, 2015 (epoch 4), respectively. C IV mini-BALs in the (a) epoch 2, (b) epoch 3 and (c) epoch 4 are compared to the C IV mini-BAL in epoch 1. Horizontal $dotted$ lines represent the normalized continuum levels.

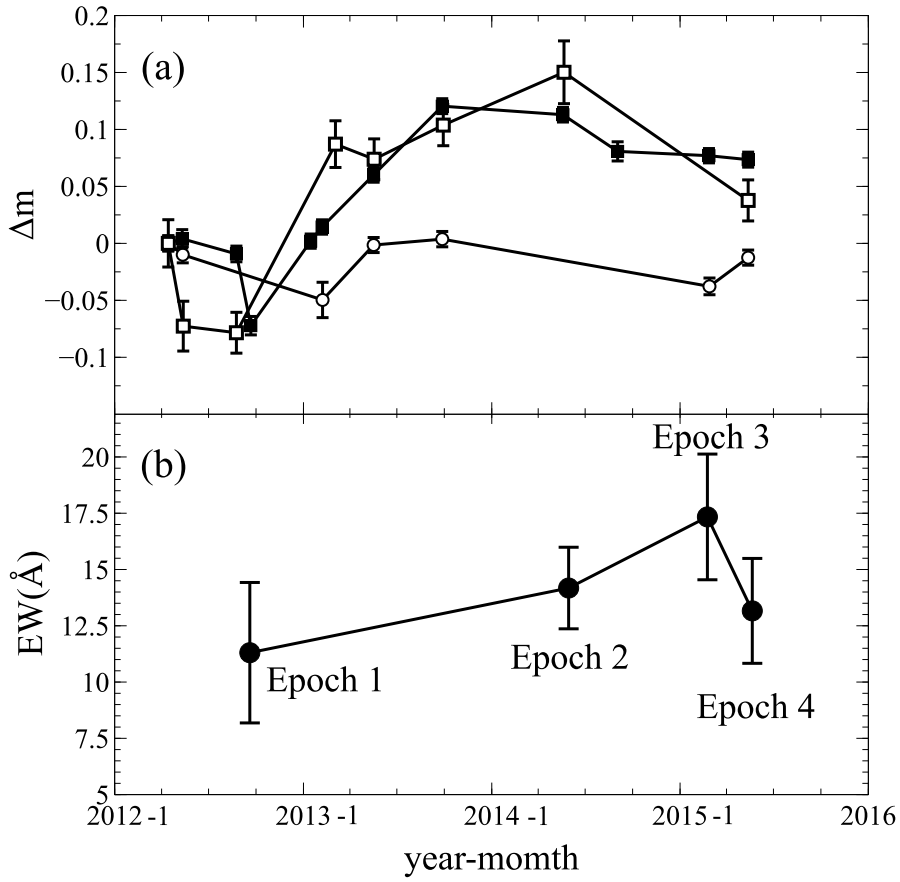

Fig. 5. (a) Light curves of SDSS u-, g-, and i-band (symbols are those of Figures 2 and 3) and (b) the EW variability of C IV mini-BAL in HS1603+3820. To clearly compare the light curves with the EW variability trend, we invert the vertical axis of Figure 2 in this figure.

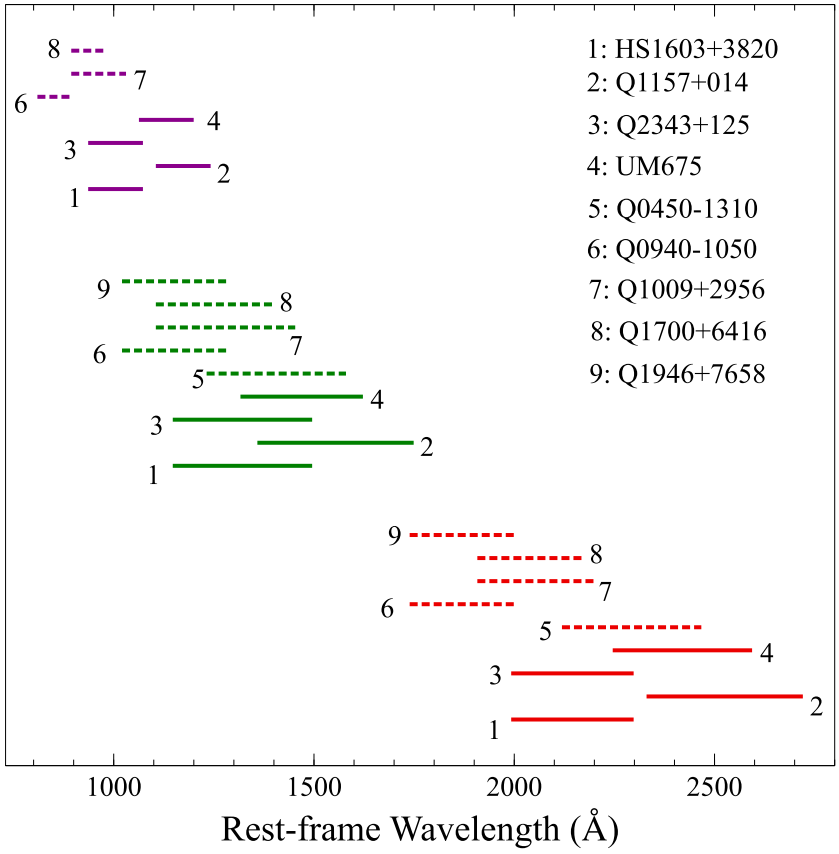

Fig. 6. Regions of rest-frame wavelength covered by SDSS u- (violet), g- (green), and i (red)-band for each quasar. $Solid$ and $Dotted$ lines represent the wavelength coverage of mini-BAL and NAL quasars, respectively. The quasars covering each wavelength range are labeled 1 - 9.

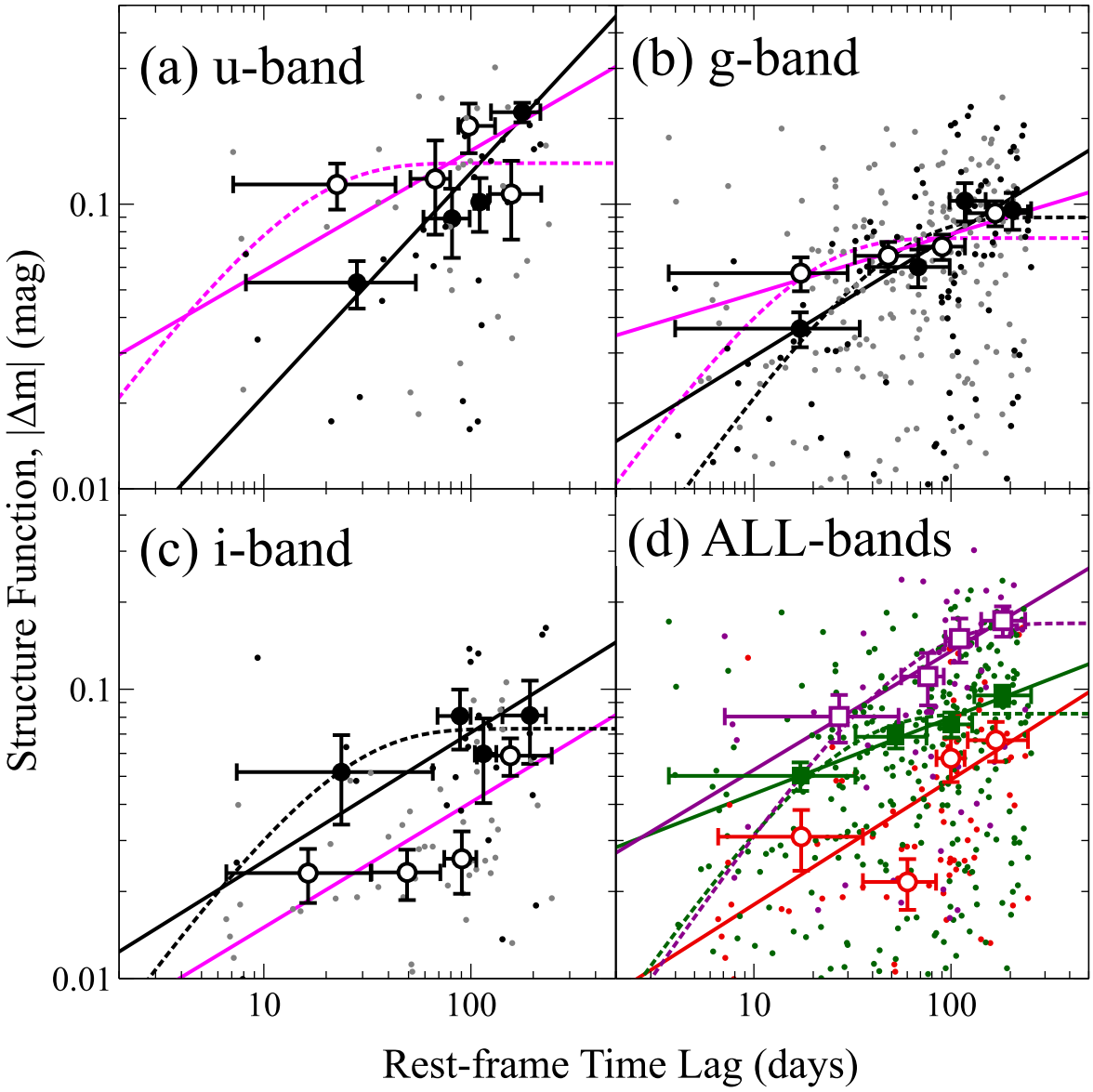

Fig. 7. Structure functions (SFs) of (a) u-band, (b) g-band , and (c) i-band of mini-BAL (filled circles) and NAL (open circles) quasars, plotted on a log - log scale. The statistical error in the SF includes the error propagation. Horizontal error bars indicate the variances from the mean time intervals in each bin. In panels (a), (b), and (c), the quasar variabilities of mini-BAL (black dots) and NAL (gray dots) quasars are plotted for all combinations of the observing epochs. The SFs of the mini-BAL (black lines) and NAL (magenta lines) quasars are fitted by a power low ($solid\ line$) and an asymptotic function ($dotted\ line$), respectively. (d) The SFs of all subsamples including mini-BAL and NAL quasars in the u-band (violet), g-band (green) and i-band (red) are also fitted to power-law and asymptotic functions. The quasar variabilities of all our quasars in u-band (violet dots), g-band (green dots), and i-band (red dots) are also plotted for all combinations of the observing epochs. Unsatisfactory fitting results are omitted.

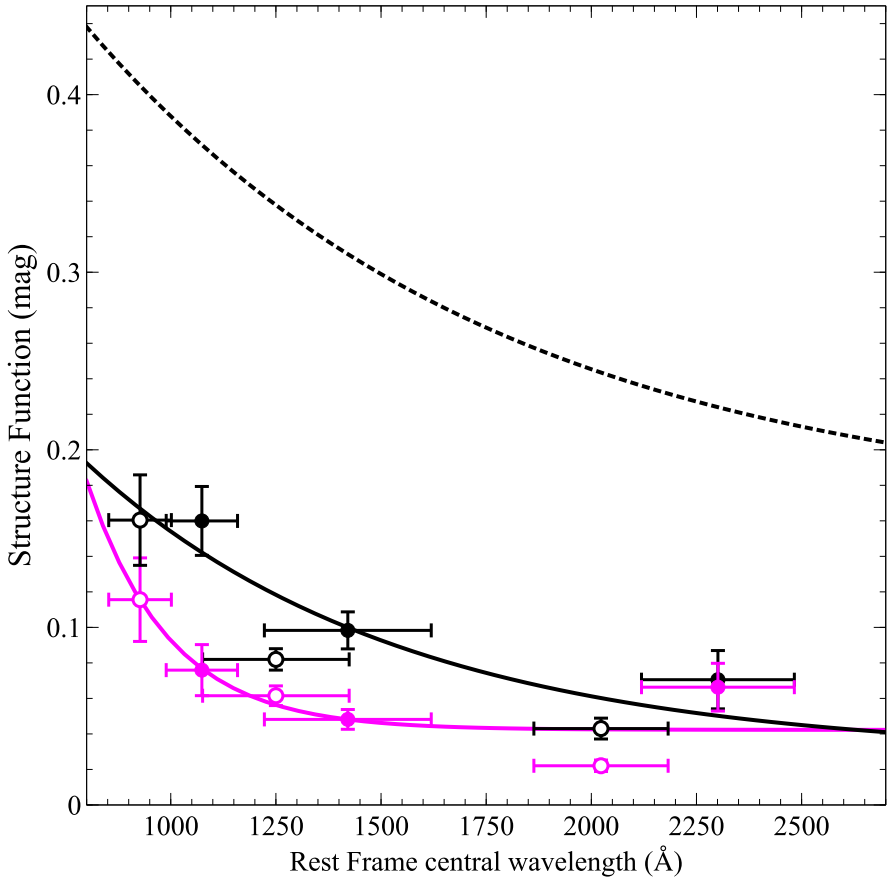

Fig. 8. Structure function versus rest-frame wavelength. The samples were first separated into two subsamples with longer and shorter time-lags. The separation criterion was $\Delta\tau$ = 90 days in the rest-frame. Filled and open circles (magenta: $\Delta\tau < 90$, black: $\Delta\tau > 90$) indicate the SFs of mini-BAL and NAL quasars, respectively. For each mini-BAL / NAL quasar, the rest-frame central wavelength denotes the average central (rest-frame) wavelengths among all bands. Horizontal error bars indicate the bandwidth of each filter. *Solid* black ($\Delta\tau > 90$) and magenta ($\Delta\tau < 90$) curves are the fitting results. Black $dotted$ curve is fitted to the $\sim$25000 normal quasars from VB04 data by Eq. (7) ($A = 0.616 \pm 0.056$, $\lambda_0 = 988 \pm 60$, $B = 0.164 \pm 0.003$).

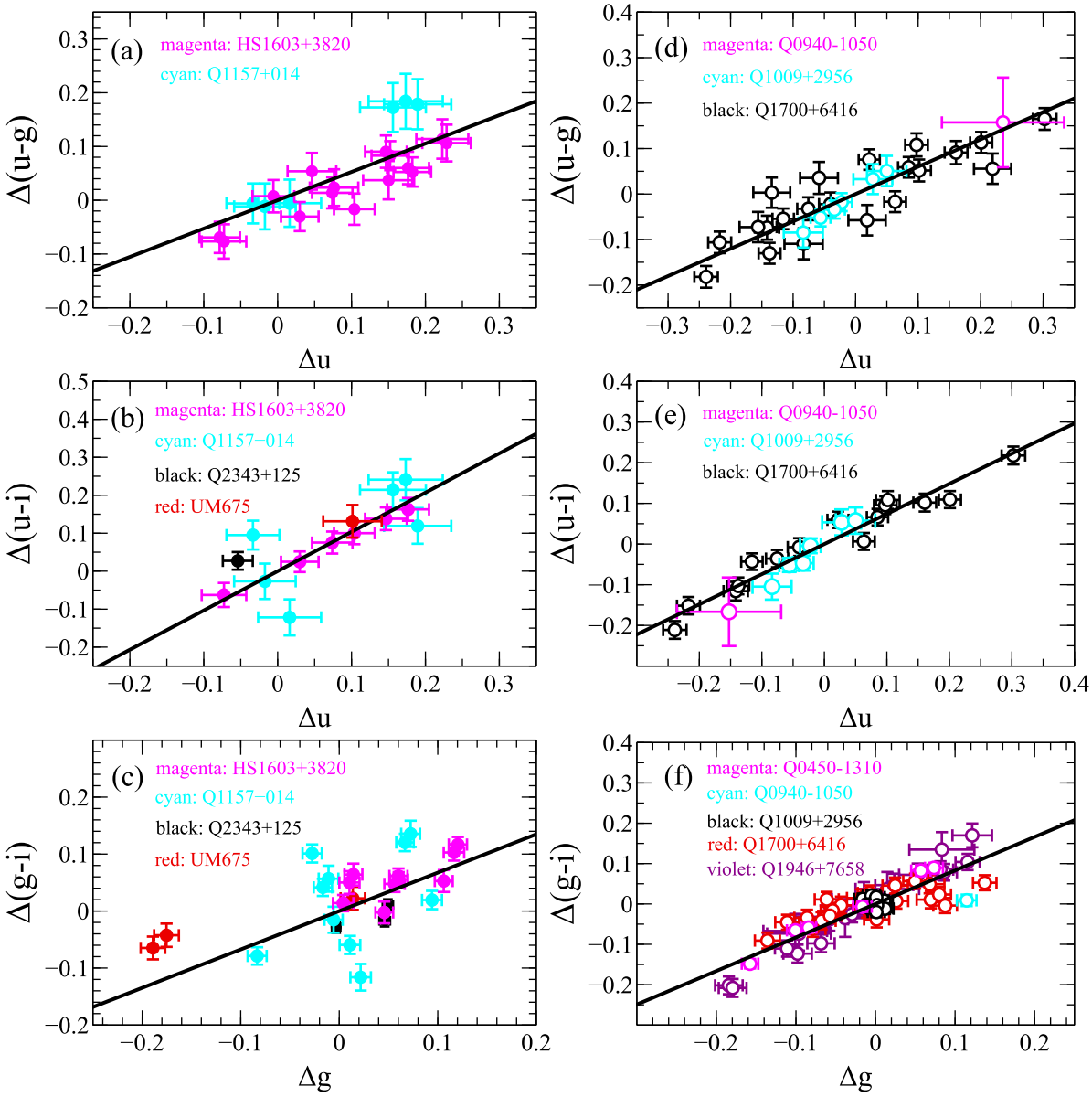

Fig. 9. Color variability of $\Delta(u-g)$ (top), $\Delta(u-i)$ (middle) and $\Delta(g-i)$ (bottom) versus magnitude variability in mini-BAL (left column: (a), (b), and (c)) and NAL (right column: (d), (e), and (f)) quasars. Magnitude variabilities were determined in the bluer bands. Solid lines are the best fits to the distributions.

Table 1. Sample Quasars

Quasar	RA*	Dec†	$m_{\rm V}$ ($M_{\rm V}$)‡ (mag)	$z_{\rm em}^{\S}$	$z_{\rm abs}^{\|}$	$v_{\rm ej}^{\#}$ (km s^{-1})	Variability**	$\langle {\rm EW}_{\rm abs,CIV}\rangle^{\dagger\dagger}$ (Å)	$\langle\Delta{\rm EW}\rangle^{\ddagger\ddagger}$	$(\Delta{\rm EW})_{\rm max}^{\S\S}$	$R^{\|\|\|}$	$\log L_{\rm bol}^{\#\#}$	$\log M_{\rm BH}/M_\odot$***	$\varepsilon^{\dagger\dagger\dagger}$	Ref. ‡‡‡
mini-BAL Quasar															
HS1603+3820	16:04:55.4	+38:12:01	15.99 (−30.60)	2.542	∼2.43	∼9500	Y	13.10	2.03±0.38	7.83±2.16	<0.2	48.27	9.72	2.87	1,5,8
Q1157+014	11:59:44.8	+01:12:07	17.52 (−28.49)	2.00	∼1.97	∼3000	Y§§§	37.96	1.09±1.21	1.41±1.61	471	47.47	9.14	1.70	2,5,2
Q2343+125	23:46:28.2	+12:49:00	17.0 (−29.62)	2.515	∼2.24	∼24400	N	2.48	0.84±0.48	1.25±0.82	1.27	47.87	9.08	4.90	11,5,9
UM675	01:52:27.3	−20:01:06	17.4 (−28.81)	2.15	∼2.13	∼1900	Y	4.51	—lll	1.54±0.32	438	47.58	9.52	0.91	3,5,10
NAL Quasar															
Q0450-1310	04:53:13.6	−13:05:55	16.5 (−29.89)	2.300	2.2307	37037	N	—	—	—	<1.69	48.01	9.59	1.90	4,12,12
Q0940-1050	09:42:53.4	−11:04:25	16.90 (−30.26)	3.080	2.8347	18578	N	1.64	0.03±0.04	0.04±0.06	<2.58	48.11	9.48	3.59	4,12,12
Q1009+2956	10:11:56.6	+29:41:41	16.05 (−30.71)	2.644	2.2533	33879	N	1.73	—lll	0.01±0.07	<1.58	48.49	9.53	7.21	4,6,8
Q1700+6416	17:01:00.6	+64:12:09	16.17 (−30.66)	2.722	2.7125	767	N	0.30	0.02±0.01	0.03±0.02	<1.24	48.98	10.4	3.02	4,6,2
Q1946+7658	19:44:55.0	+77:05:52	16.20 (−30.94)	3.051	2.8928	927	N	0.29	—###	—###	<1.35	48.38	10.23	1.12	4,7,7

Notes — * Right Ascension. † Declination. ‡ V-band magnitude (Vega) from Véron-Cetty and Véron (2010). Values in parentheses are absolute magnitudes. § C IV emission redshift. ‖ Apparent redshift of C IV outflow. # Ejection velocity determined from the quasar emission redshift (in km s^{-1}). ** Absorption line variability (Yes or No). See Misawa, Charlton and Eracleous (2014). †† Averaged equivalent width of C IV absorption line given by the outflows (in Å), from Misawa, Charlton and Eracleous (2014). ‡‡ Averaged amplitude of C IV absorption variabilities, from Misawa, Charlton and Eracleous (2014). §§ Maximum amplitude of C IV absorption variabilities, from Misawa, Charlton and Eracleous (2014). ‖‖ Radio loudness. ## Bolometric luminosity. *** Central black hole mass (in units of solar units). ††† Eddington ratio, $L_{\rm bol}/L_{\rm Edd}$. ‡‡‡ References for R, $\log L_{bol}$, and $\log M_{BH}$ in numerical order — (1) Just et al. (2007), (2) Shen et al. (2011), (3) Griffith et al. (1994), (4) Misawa et al. (2007a), (5) Misawa, Charlton and Eracleous (2014), (6) Wu et al. (2010), (7) Kuhn et al. (1995), Różańska et al. (2014), (9) Trainor and Steidel (2012), (10) Dietrich et al. (2009), (11) FIRST survey, and (12) This paper. §§§ Variability is seen only in Si IV mini-BAL with a significance level of $\sim 2.4\sigma$ (Misawa, Charlton and Eracleous 2014). lll Cannot be calculated because our sample was limited to two epochs. ### We cannot calculate these because C IV NAL was observed only once (Misawa, Charlton and Eracleous 2014).

Table 2. Log of observations

QSO	Obs-Date (day)	Band	$\Delta t^{*}_{\rm rest}$ (s)	$t^{\dagger}_{\rm EXP}$
HS1603+3820 (mini-BAL QSO)	2012 Apr 14	u	0	180×5
	2012 Apr 14	g	0	60×5
	2012 Apr 14	i	0	60×5
	2012 May 12	i	7.9	60×5
	2012 May 12	g	8.2	60×5
	2012 May 13	u	8.2	300×5
	2012 Aug 24	u	37.3	300×5
	2012 Aug 24	g	37.3	60×3
	2012 Sep 21	g	45.2	180×3
	2013 Jan 15	g	77.9	180×5
	2013 Feb 6	g	84.1	60×5
	2013 Feb 7	i	84.4	300×3
	2013 Mar 4	u	91.5	300×3
	2013 May 17	g	112.4	60×5
	2013 May 17	i	112.4	60×5
	2013 May 18	u	112.6	420×1, 480×3, 600×1
	2013 Sep 27	g	149.9	120×5
	2013 Sep 27	i	149.9	120×5
	2013 Sep 29	u	150.5	300×5
	2014 May 19	g	215.0	60×5
	2014 May 21	u	216.5	300×4
	2014 Sep 2	g	245.9	120×2, 180×2, 240×1
Q1157+014 (mini-BAL QSO)	2012 Apr 14	u	0	300×5
	2012 Apr 14	g	0	120×5
	2012 Apr 14	i	0	60×1, 120×4
	2012 May 12	u	9.3	300×5
	2012 May 12	g	9.3	120×5
	2012 May 12	i	9.3	120×5
	2013 Jan 15	g	92	180×1, 300×5
	2013 Feb 6	g	99.3	180×5
	2013 Mar 3	g	107.7	180×5
	2013 Mar 3	i	107.7	180×3
	2013 Mar 4	u	108.0	600×3
	2013 May 17	g	132.7	120×5
	2013 May 17	i	132.7	120×5
	2013 Dec 10	u	201.7	600×4
	2013 Dec 10	g	201.7	360×3
	2013 Dec 10	i	201.7	180×5
	2014 May 19	g	255.0	120×5
Q2343+125 (mini-BAL QSO)	2012 Aug 25	g	0	120×1, 180×1, 240×1
	2012 Sep 8	g	4.0	120×5
	2012 Oct 21	g	16.2	120×5
	2012 Oct 21	i	0	120×5
	2012 Nob 16	g	23.6	120×4
	2012 Nob 16	i	7.4	120×5
	2013 Sep 27	g	113.2	120×4, 240×1
	2013 Sep 27	i	97.0	120×5
	2013 Sep 28	u	0	300×5

Table 2. (Continued)

QSO	Obs-Date (day)	Band	$\Delta t^{*}_{\rm rest}$ (s)	$t^{\dagger}_{\rm EXP}$
	2014 Sep 2	g	209.9	120×1, 180×4
	2014 Oct 16	u	109.0	300×1, 360×4
	2014 Oct 16	g	222.5	120×5
	2014 Oct 16	i	206.2	120×4
UM675 (mini-BAL QSO)	2012 Aug 26	g	0	300×2
	2012 Sep 8	g	4.1	120×5
	2012 Oct 21	g	17.8	120×5
	2012 Oct 21	i	0	120×5
	2012 Nob 17	g	26.0	120×4
	2012 Nob 18	i	8.9	120×5
	2013 Sep 27	g	126.0	180×1, 240×3
	2013 Sep 28	u	0	420×5
	2013 Sep 28	i	108.6	120×5
	2014 Sep 2	g	234.0	180×3
	2014 Oct 16	u	121.6	300×2
	2014 Oct 16	i	230.2	120×4
Q0450-1310 (NAL QSO)	2012 Sep 9	g	0	60×2, 120×3
	2012 Oct 20	g	12.4	60×3, 120×2
	2012 Oct 20	i	0	120×5
	2012 Nob 17	g	20.9	180×3
	2012 Nob 18	i	8.8	60×5
	2013 Feb 6	g	45.4	180×2, 240×1
	2013 Sep 27	g	116.0	120×5
	2013 Sep 27	i	103.6	60×5
	2013 Dec 10	g	138.5	240×5
	2013 Dec 10	i	126.1	60×5
Q0940-1050 (NAL QSO)	2012 Apr 14	u	0	300×5
	2012 Apr 14	i	0	60×5
	2012 May 11	g	0	60×5
	2012 May 12	i	6.9	60×5
	2012 May 13	u	7.1	300×3
	2012 Nob 17	g	46.6	300×4, 240×1
	2013 Jan 15	g	61.0	180×5
	2013 Feb 6	g	66.4	180×5
	2013 Mar 3	g	72.5	120×5
	2013 Mar 4	u	79.4	600×2
	2013 May 17	g	90.9	60×5
	2013 Dec 10	g	142.0	180×5
	2013 Dec 10	i	148.3	120×5
Q1009+2956 (NAL QSO)	2012 Apr 14	u	0	300×5
	2012 Apr 14	g	0	60×5
	2012 Apr 14	i	0	60×4
	2012 May 11	u	8.0	300×5
	2012 May 11	g	7.4	60×5
	2012 May 12	i	7.7	60×5
	2012 Nob 18	g	59.8	180×1, 300×4
	2012 Nob 18	i	59.8	120×5
	2013 Jan 15	g	75.7	180×6

Table 2. (Continued)

QSO	Obs-Date (day)	Band	$\Delta t^{*}_{\rm rest}$ (s)	$t^{\dagger}_{\rm EXP}$
	2013 Feb 6	g	81.8	60×4, 180×1
	2013 Feb 7	i	82.0	300×5
	2013 Mar 3	g	88.6	60×4, 120×1
	2013 Mar 3	i	88.6	60×4, 120×1
	2013 Mar 4	u	88.9	300×3
	2013 May 17	g	109.2	60×5
	2013 Dec 10	u	166.0	300×5
	2013 Dec 10	g	166.0	120×5
	2013 Dec 10	i	166.0	60×5
	2014 May 19	g	209.9	60×5
Q1700+6416 (NAL QSO)	2012 Apr 14	u	0	180×5
	2012 Apr 14	g	0	60×5
	2012 Apr 14	i	0	60×5
	2012 May 11	g	7.2	60×5
	2012 May 12	i	7.5	60×5
	2012 May 13	u	7.8	300×5
	2012 Aug 25	g	35.7	120×1, 240×1, 300×1
	2012 Aug 25	i	35.7	300×3
	2012 Sep 9	g	39.8	180×2, 300×1
	2012 Oct 19	g	50.5	60×5
	2012 Oct 20	i	50.8	60×5
	2012 Oct 21	u	51.0	300×5
	2013 Jan 15	g	74.2	180×5
	2013 Feb 6	g	80.1	60×5
	2013 Mar 3	g	86.5	180×5
	2013 Mar 4	u	87.0	300×5
	2013 May 17	g	106.9	60×5
	2013 May 17	i	106.9	60×5
	2013 May 18	u	107.2	300×1, 480×1, 600×2
	2013 Sep 27	g	142.7	120×5
	2013 Sep 27	i	142.7	60×4
	2013 Sep 28	u	142.9	300×5
	2014 May 19	g	205.5	60×5
	2014 Sep 2	g	234.0	120×5
	2014 Oct 16	u	238.0	300×5
	2014 Oct 16	g	245.8	60×4, 120×1
	2014 Oct 16	i	245.0	60×1, 120×3
Q1946+7658 (NAL QSO)	2012 Apr 14	g	0	60×5
	2012 Apr 14	i	0	60×5
	2012 May 11	g	6.7	60×5
	2012 May 11	i	6.7	60×5
	2012 Aug 24	g	32.6	300×3
	2012 Aug 25	i	32.8	120×1, 300×2
	2012 Sep 8	g	36.3	60×2, 120×3
	2012 Oct 19	g	46.4	60×6
	2012 Oct 20	i	46.6	60×5
	2013 Nob 18	g	53.8	120×5
	2012 Nob 18	i	53.8	120×5

Table 2. (Continued)

QSO	Obs-Date (day)	Band	$\Delta t^{*}_{\rm rest}$ (s)	$t^{\dagger}_{\rm EXP}$
	2013 Feb 6	g	73.6	60×1, 300×2
	2013 Mar 3	g	79.7	60×5
	2013 May 17	g	98.2	60×5
	2013 May 17	i	98.2	60×5
	2013 Sep 27	g	124.4	120×1, 180×2, 240×1
	2013 Sep 28	i	131.3	60×5
	2014 May 19	g	188.8	60×5
	2014 Sep 2	g	215.0	60×1, 120×4

Notes — * Time delay from the first observation in the quasar rest-frame. Zero denotes the first epoch.
† Total exposure time for usable image, which is altered according to the weather.

Table 3. Spectroscopic observation log of HS1603+3820

Observing Epoch	Obs-Date (day)	$t^{*}_{\rm EXP}$ (s)
1	2012 Sep 19	1,200×2
2	2014 May 30	1,200×8
3	2015 Feb 23	1,200×3
4	2015 May 21	1,200×3

* Total exposure time for usable image.

Table 4. Detailed variability properties of the light curves of min i-BAL and NAL quasars

Quasar	Type	N^*	σ_m † (mag)	$\langle\|\Delta m\|\rangle$‡ (mag)	$\|\Delta m_{\rm max}\|$§ (mag)	$\langle\|\Delta m/\Delta t_{\rm rest}\|\rangle$‖ (mag/yr)	$\|\Delta m/\Delta t_{\rm rest}\|_{\rm max}$# (mag/yr)
SDSS u-band							
HS1603+3820	mini-BAL QSO	7	0.068	0.104±0.015	0.229±0.035	0.387± 0.040	1.116±0.204
Q1157+014	mini-BAL QSO	4	0.084	0.086±0.033††	0.189±0.045	0.285±0.070	0.676±0.196
Q2343+125	mini-BAL QSO	2	— **	— **	0.054±0.020††	— **	0.181±0.068††
UM675	mini-BAL QSO	2	—**	—**	0.101±0.040††	—**	0.304±0.119††
Q0940-1050	NAL QSO	3	0.080	0.138±0.042	0.236±0.098††	0.634±0.402	1.191±0.496††
Q1009+2956	NAL QSO	4	0.023	0.041±0.008	0.056±0.016	0.116±0.028	0.123±0.035
Q1700+6416	NAL QSO	7	0.076	0.128±0.017	0.302±0.019	0.326±0.063	3.546±0.831
SDSS g-band							
HS1603+3820	mini-BAL QSO	10	0.049	0.069±0.007	0.193±0.009	0.229 ±0.021	2.909±0.451
Q1157+014	mini-BAL QSO	8	0.030	0.040±0.005	0.094±0.010	0.109±0.020	1.549±0.358
Q2343+125	mini-BAL QSO	7	0.020	0.023±0.004	0.067±0.001	0.042±0.014	4.634±0.058
UM675	mini-BAL QSO	6	0.083	0.110±0.021	0.220±0.017	0.334±0.041	0.691±0.045
Q0450-1310	NAL QSO	6	0.047	0.070±0.012	0.158±0.010	0.301±0.056	2.568±0.169
Q0940-1050	NAL QSO	7	0.028	0.046±0.006	0.115±0.012	0.304±0.023	0.929±0.196
Q1009+2956	NAL QSO	9	0.014	0.015±0.002	0.054±0.011	0.052±0.009	0.303±0.080
Q1700+6416	NAL QSO	13	0.044	0.069±0.005	0.170±0.016	0.193±0.019	9.248±1.545
Q1946+7658	NAL QSO	12	0.052	0.076±0.007	0.237±0.017	0.249±0.033	16.900±1.778
SDSS i-band							
HS1603+3820	mini-BAL QSO	5	0.024	0.012±0.005††	0.053±0.016	0.033±0.020††	0.630±0.208
Q1157+014	mini-BAL QSO	5	0.065	0.065±0.013	0.138±0.021	0.145±0.050††	5.027±0.4887
Q2343+125	mini-BAL QSO	2	0.024	0.044±0.009	0.081±0.011	0.117±0.040††	0.238±0.032
UM675	mini-BAL QSO	4	0.066	0.102±0.027	0.163±0.017	0.273±0.043	0.456±0.058
Q0450-1310	NAL QSO	4	0.010	0.020±0.004	0.035±0.005	0.086±0.009	0.090±0.019
Q0940-1050	NAL QSO	3	0.052	0.083±0.025	0.105±0.007	0.254±0.011	0.260±0.017
Q1009+2956	NAL QSO	6	0.008	0.014±0.002	0.028±0.007	0.049±0.013	0.174±0.046
Q1700+6416	NAL QSO	7	0.024	0.042±0.005	0.092±0.007	0.119±0.018	1.934±0.392
Q1946+7658	NAL QSO	7	0.014	0.020±0.003	0.051±0.014	0.094±0.020	0.674±0.220

Notes — * Number of observing epochs.
† Standard deviation of magnitude of mini-BAL and NAL quasars.
‡ Mean quasar variability.
§ Maximum quasar variability.
‖ Mean quasar variability gradient in the quasar rest-frame.
Maximum quasar variability gradient in the quasar rest-frame.
** Cannot be calculated because our sample was limited to two epochs.
†† Confidence level of quasar variability is below than 3σ.

Table 5. Observed frame equivalent width of C IV mini-BAL in the HS1603+3820 spectrum

Observing Epoch*	v_{shift} (km s^{-1})	$\Delta t^{\dagger}_{\rm rest}$	$\mathrm{EW}^{\ddagger}_{\mathrm{C\,IV}}$ (Å)	Detection Significance
1	$\sim 9,500$	0	11.3±3.1	3.6σ
2		180.2	14.2±1.8	7.8σ
3		258.6	17.3±2.8	6.2σ
4		284.0	13.2±2.3	5.6σ

Notes — * Defined as in Table 3. † Time delay from the first observation in the absorber rest-frame. Zero denotes the first observation epoch. ‡ Equivalent width of C IV mini-BAL in the observed frame.

Table 6. Power-law and asymptotic fitting parameters of structure functions

Quasars	Authors	S_p		S_a	
		γ	$S(\Delta\tau$ =100d) (mag)	$\Delta\tau_a$ (Asymptotic) (day)	V_a (mag)
SDSS u-band					
mini-BAL quasars	this work	0.785±0.109	0.129±0.037	—†	—†
NAL quasars	this work	0.422±0.345	—*	12.282±10.090	0.139±0.026
All of our quasars	this work	0.410±0.115	0.135±0.076	49.362±15.210	0.169±0.019
SDSS 7886 quasars	W08	0.435	0.173±0.001	—	—
SDSS g-band					
mini-BAL quasars	this work	0.426±0.078	0.078±0.036	37.980±15.640	0.090±0.016
NAL quasars	this work	0.210±0.071	0.078±0.067	13.537±6.981	0.076±0.008
All of our quasars	this work	0.264±0.056	0.080±0.043	20.768±7.478	0.082±0.008
SDSS 25,710 sample	VB04	0.293± 0.030	—	51.9±6.0‡	0.168±0.005
SDSS 7886 quasars	W08	0.479	0.147±0.001	—	—
SDSS i-band					
mini-BAL quasars	this work	0.446±0.263	—*	18.870±9.088	0.073±0.008
NAL quasars	this work	0.432±0.111	—*	—*	—*
All of our quasars	this work	0.432±0.121	—*	—†	—†
SDSS 25,710 sample	VB04	0.303±0.035	—	62.6±8.3‡	0.139±0.005
SDSS 7886 quasars	W08	0.436	0.108±0.001	—	—

Notes — * Unphysical values were obtained.
† The data cannot be properly fitted by an asymptotic function.
‡ Data in VB04 not explicitly given to two decimal places.

Table 7. Distribution properties of color variability versus quasar variability

Distribution	N^*	$r^\dagger$	$a^\ddagger$
mini-BAL Quasar			
$\Delta(u-g)$-Δu	21	0.821	0.527±0.064
$\Delta(u-i)$-Δu	14	0.781	1.034±0.121
$\Delta(g-i)$-Δg	26	0.570	0.674±0.048
NAL Quasar			
$\Delta(u-g)$-Δu	28	0.891	0.601±0.041
$\Delta(u-i)$-Δu	22	0.962	0.741±0.042
$\Delta(g-i)$-Δg	64	0.882	0.830±0.038

Notes — * Number of data points.
† Pearson product-moment correlation coefficient.
‡ Slope of regression line.

Table 8. Color variability properties of mini-BAL and NAL quasars

Color	$\sigma^*_{\Delta c}$ (mag)	$\langle\Delta C\rangle^\dagger$ (mag)	$\lvert\Delta C_{\rm max}\rvert^\ddagger$ (mag)	Quasar§	$\langle\Delta C/\Delta t_{\rm rest}\rangle^\parallel$ (mag/yr)	$(\lvert\Delta C/\Delta t_{\rm rest}\rvert)^\#_{\rm max}$ (mag/yr)	Quasar**
mini-BAL Quasar							
$\Delta(u-g)$	0.057	0.058±0.010	0.184±0.051	Q1157+014	0.161±0.040	0.718±0.200	UM675
$\Delta(u-i)$	0.069	0.092±0.016	0.241±0.046	Q1157+014	0.305±0.048	0.482±0.104	HS1603+3820
$\Delta(g-i)$	0.038	0.051±0.007	0.136±0.023	Q1157+014	0.174±0.028	3.952±0.621	Q1157+014
NAL Quasar							
$\Delta(u-g)$	0.047	0.071±0.009	0.182±0.025	Q1700+6416	0.170±0.034	1.956±0.609	Q1700+6416
$\Delta(u-i)$	0.060	0.080±0.013	0.218±0.022	Q1700+6416	0.188±0.046	1.374±0.129	Q1700+6416
$\Delta(g-i)$	0.049	0.048±0.006	0.208±0.022	Q1946+7658	0.107±0.025	5.329±0.584	Q1946+7658

Notes — * Standard deviation of color amplitude.
† Mean amplitude of color variability.
‡ Maximum amplitude of color variability.
§ Quasar with maximum color variability amplitude.
‖ Mean color variability gradient (per year).
Maximum color variability gradient (per year).
** Quasar with maximum color variability gradient.